SCIENTIFIC REPORTS
nature research

OPEN

Evidence of radial Weibel instability in relativistic intensity laser-plasma interactions inside a sub-micron thick liquid target

Gregory K. Ngirmang[1,6]✉, John T. Morrison[2], Kevin M. George[2], Joseph R. Smith[3], Kyle D. Frische[2], Chris Orban[3], Enam A. Chowdhury[4,5] & W. Mel Roquemore[6]

Super-intense laser plasma interaction has shown great promise as a platform for next generation particle accelerators and sources for electron, x-rays, ions and neutrons. In particular, when a relativistic intense laser focus interacts with a thin solid density target, ionized electrons are accelerated to near the speed of light (*c*) within an optical cycle and are pushed in the forward and transverse directions away from focus, carrying a significant portion of the laser energy. These relativistic electrons are effectively collisionless, and their interactions with the ions and surrounding cold electrons are predominantly mediated by collective electromagnetic effects of the resulting currents and charge separation. Thus, a deeper understanding of subsequent high energy ions generated from various mechanisms and their optimization requires knowledge of the relativistic electron dynamics and the fields they produce. In addition to producing MV/m quasi-static fields, accelerating the ions and confining the majority of the electrons near the bulk of the laser target, these relativistic electron currents are subject to plasma instabilities like the Weibel instability as they propagate through the thermal population in the bulk target. In this work, we present high temporal (100 fs) and spatial (1 μm) resolution shadowgraphy video capturing relativistic radial ionization front expansion and the appearance of filamentation radiating from the laser spot within a sub-micron thick liquid sheet target. Filamentation within the region persists for several picoseconds and seeds the eventual recombination and heating dynamics on the nanosecond timescale. A large scale three-dimensional particle-in-cell (PIC) simulation of the interaction revealed the presence of strong magnetic fields characteristic of Weibel Instability, and corroborated the relativistic radial expansion of the ionization front, whose speed was determined to be 0.77*c*. Both the experimental and simulation results strongly point towards the target field ionization and the outward expanding hot electron current as the cause of the radial expansion.

The development of chirped pulse amplification[1] has led to a dramatic increase in the intensity of ultrashort pulse laser systems. As a result, the study of extreme phenomena stemming from the interaction of relativistically intense lasers with matter has produced a rich field of research with broad and promising applications. Relativistic laser-plasma interactions (RLPI) generate exotic states of warm dense matter, accelerate charged particles to relativistic energies[2–5], and drive fundamental plasma processes rarely observed in nature.

Examination of the RLPI event remains a challenge given the femtosecond-temporal and submicron-spatial scale evolution of the interaction. A variety of experimental techniques have been developed in an effort to better understand and diagnose these conditions[6–10]. Nonetheless, the difficulty of resolving these temporal and spatial scales necessitate the use of computational particle-in-cell (PIC) simulations to model the RLPI physics of these scales directly. These codes which model RLPI with unprecedented detail are one of the few accepted methods

[1]National Academies of Sciences, Engineering, and Medicine, Washington, DC, USA. [2]Innovative Scientific Solutions, Inc., Dayton, Ohio, 45459, USA. [3]Ohio State University, Department of Physics Columbus, Ohio, 43210, USA. [4]Intense Energy Solutions, LLC., Plain City, Ohio, 43064, USA. [5]Ohio State University, Department of Material Science and Engineering, Ohio, 43210, USA. [6]Air Force Research Laboratory, Dayton, Ohio, 45433, USA. ✉e-mail: ngirmang@protonmail.com

to fully resolve these scales and play an important role explaining the underlying physics in these extreme conditions, although they represent an indirect probe of the experimental physics through corroboration with observation.

Utilizing a novel pump-probe imaging system, detailed in Feister *et al.*[10], we generate time resolved movies of the RLPI with high temporal (100 femtosecond) and spatial (1 micron) resolution. With this technique, we observe the evolution of a hot electron induced, above critical density plasma expansion, radially oriented from the laser-target interaction region within a 450 nm thick liquid sheet target. Plasma instabilities lead to the formation of radially oriented filaments, which are initiated by what we believe to be a Weibel instability[11], forming between the expanding hot electron population from the laser spot radially outward and the counterpropagating neutralizing, cold, return current. Fully three-dimensional PIC modeling corroborate these findings with the presence and growth of strong, radially oriented, alternating magnetic fields within the target.

Previous works have reported the occurrence of Weibel instabilities and filamentation driven by RLPI generated hot electrons, though mostly in a linear geometry through the thickness of the target. This geometry is predominantly relevant to electron transport[12–18] and as well as filamentation in laser accelerated protons beams[19–21]. To distinguish this work's geometry from the former longitudinal case, we refer to it as the "radial Weibel instability." For the sake of clarity, we are referencing the experimental geometry and not the direction of the anisotropy or *k*-vector of the instability. The implications of the radially oriented filamentation upon which we report is expected to be widespread given the common experimental conditions of a high-intensity laser incident onto a submicron thick planar target, but has not garnered significant emphasis. Although previous simulation and theoretical developments by Schoeffler and Silva[22] and other works by this group[23–25] consider a radially oriented velocity anisotropy, Weibel instability generation in this geometry has not been widely accounted for in the literature. A closer analog of the observed filaments in this article are filaments formed from the expansion of an irradiated wire, which was observed by Quinn *et al.*[26]. The observation of radial filaments in this geometry implicates the non-uniform heating in the bulk target and imprinting of the filamentation pattern on lower energy target normal sheath accelerated ions[27], which are two active areas of interest relevant for high energy density physics generally, especially as state of the art systems push the intensity frontier. Lastly, it is important to highlight that this result was only made possible by the combination of several systems unique to the field of RLPI; short pulse pump-probe imaging scheme, high-repetition rate relativistically intense laser, transparent sub-micron thick liquid target, and real time diagnostic feedback. This observation of ~40 μm long radial filaments, subsequent features persisting 100's of ps, and their repeatability over thousands of shots in a kHz pulse train is facilitated by the employment of this novel target and accompanying repetition rate capable diagnostics and experiment. (See Supplemental Videos for more detail.)

Results

Observation of radial filamentation. We present the observation of laser plasma surface expansion and the filamentation of this laser produced plasma in a sub-micron thick target, corroborated by the development of a radial Weibel instability in three-dimensional high resolution Particle-in-Cell (PIC) simulations. The experiment, displayed in Fig. 1a, was performed with a relativistic intensity, short pulse laser incident on a thin (~0.5 μm) target[28]. The laser-target interaction was illuminated by a short pulse probe beam created from frequency doubling different pulses of a common oscillator in a scheme described in the Feister *et al.*[10] and in the Methods section. The use of a common oscillator allows the synchronization of the shadowgraphy with the main pulse. Utilizing the repetition rate, we develop time resolved movies of the target evolution, a frame of which is shown in Fig. 1b and is supplied in the Supplemental Data. We interpret the darkening of the target as attenuation of the probe beam due to free electron density, and therefore serves as a measurement of the electron dynamics. On the outer edge of the dark spot, finger like features are present, suggesting that the electron density is filamented as it expands. We posit that as the ionization front moves radially away from the target, an electromagnetic instability results as the cold electron return current counter propagates. The instability we suggest is similar to the Weibel instability given that the wavenumber of the filaments are normal to the direction of hot electron motion which is radially away from the laser spot. This perspective was substantiated by PIC simulations that modelled the initial laser target interaction. The free electron density in the target plane is found to filament femtoseconds after irradiation as shown in Fig. 1c, and plots of the magnetic field component into and out of the target in Fig. 1d demonstrates a quasi-static pinching of the filaments, consistent with simulations of the Weibel instability in previous work in linear geometry (see for example, Fig. 5 of Tatarakis *et al.*[18], Fig. 1 of Sentoku *et al.*[12], Fig. 4 of Wei *et al.*[29], Fig. 3 of Göde *et al.*[30]) as well as work by Schoeffler *et al.* in a radial geometry[22,24] (see in particular Fig. 3 of Schoeffler and Silva[22]).

Temporal shadowgraphy movie. Figure 2 displays frames from the movies, showing the full time resolved nature of this measurement, particularly highlighting the evolution of the ionization front. The features develop as follows. First, in just hundreds of femtoseconds after the first feature of darkening appears, a rapidly expanding filament like feature develops across the target in the direction of the *k*-vector along the target surface. Coincident with the filamentation is the initial expansion of a darkened region. After half a picosecond, the darkened patch grows and becomes apparent, with filaments also becoming discernible near the edges of the dark spot. We recommend that the reader view the video included in the supplement in order to better understand the feature we observe and describe here.

It should be highlighted how the experimental observation of the dark feature and its evolution was facilitated by the time resolved nature of the movies. The diagnostic provides a means to observe the target evolution over a large range of timescales, from the picosecond to the nanosecond scale after the target interaction. This facilitated discovery of the feature which would have required either foreknowledge[22] or chance. Moreover, the movie creation scheme detailed in the Methods section stitches together images from different main pulse shots into a single movie, and mere observation

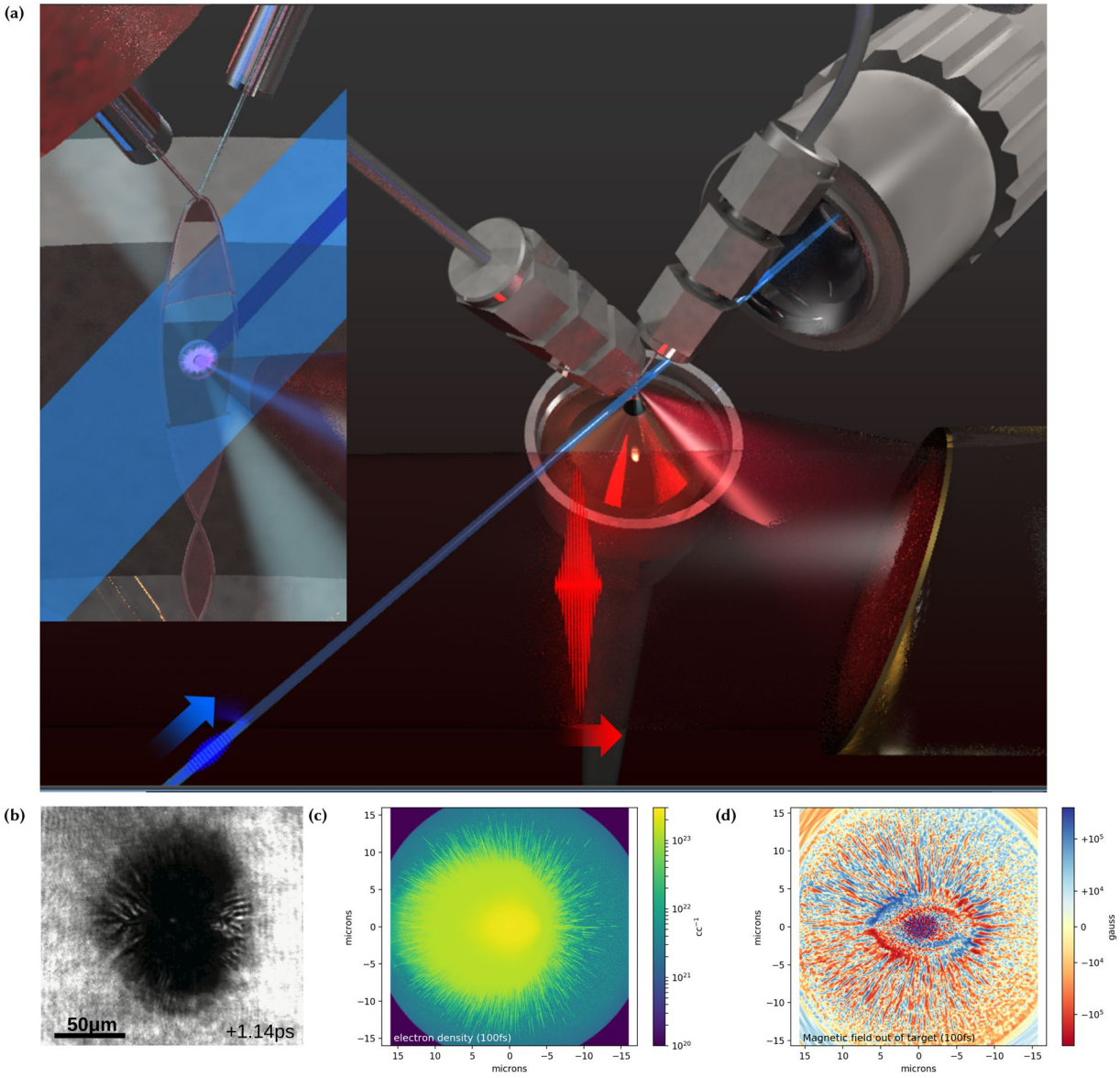

Figure 1. (**a**) Schematic of experimental setup employed to view the Weibel instability formation and evolution within a sub-micron thin, free flowing liquid sheet. A 420 nm and 80 fs pulse duration probe beam is synchronized and perpendicular to the 5 mJ, 40 fs main pulse with 780 nm wavelength. A variable delay was used to illuminate the sheet viewed at 45° with a 10× microscope objective. This system is capable of temporal resolution of 100 fs and arbitrary pump-probe delay. (**b**) Frame of the shadowgraphy movie that demonstrates the filamentation feature. (**c**) Particle-in-Cell free electron density illustrates the initial formation of the filamentation feature. (**d**) Magnetic field component out of the target plane in the Particle-in-Cell simulations demonstrating pinching around the filaments. Videos are provided in the Supplemental Data, and zoomed in snapshots of (**c**,**d**) for the sake of detailed comparison are included in the Supplemental Figures. The computational sub-figures (**c**,**d**) were produced using Matplotlib[46].

of the stability of a feature in the video allows an immediate gauge of the repetability and shot-to-shot stability of the feature in the experiment. The filamentary structures we observe are stable when viewed as a video, implying that the seed of these filaments is non-random and repeatable. This fact will be discussed in the following section. Finally, although not shown in Fig. 2 one can observe the later time hydrodynamic explosion of the target nanoseconds after the RLPI in the movies provided in the supplement, demonstrating the large temporal range provided by this technique.

Discussion

Seeding of the instability. As discussed previously, the filaments in these videos appear consistent in shape and darkness, and thus appear "stable" when viewed as a movie as can be observed in the Supplementary Video. Given the pump-probe method that takes snapshots across different shots, this means that the filaments are in fact the *same* in configuration from shot-to-shot. This suggests that the instability process that leads to filamentation

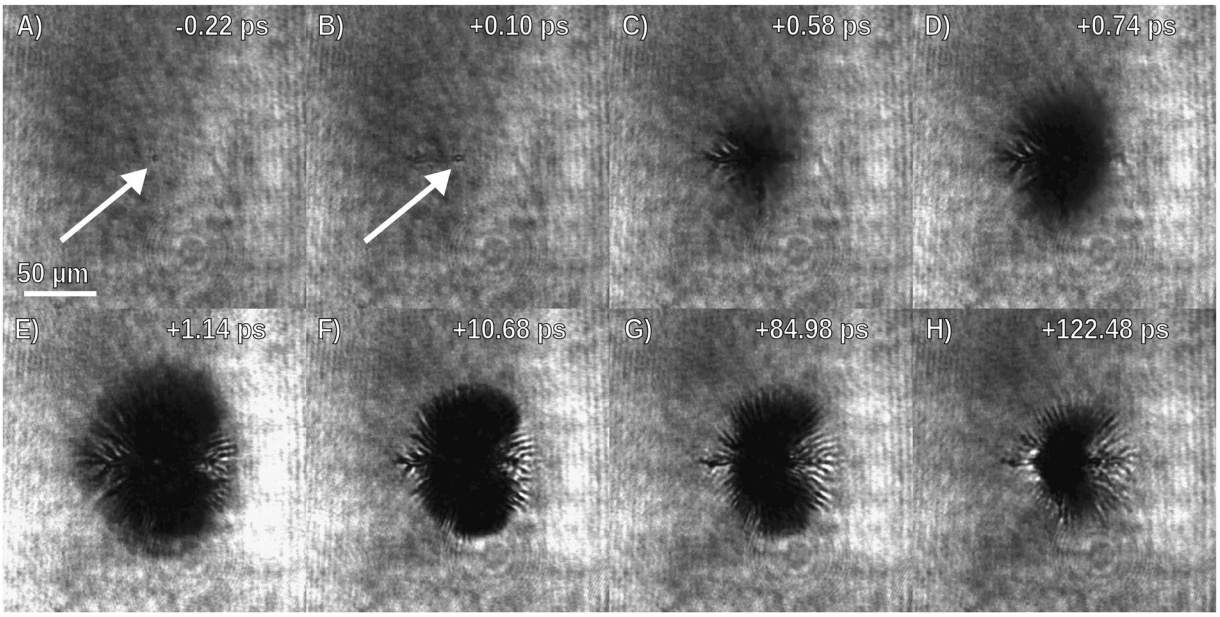

Figure 2. Short pulse probe beam shadowgraphic microscope images of the evolution of filaments and ionization from expanding energetic electrons within the thin liquid sheet (video provided in the Supplemental Data). Images are integrated over the ~80 fs duration of the probe, and times are ±100 fs. (**A**) Preceeding the arrival of the main pulse, the target surface is perturbed by prepulse on the picosecond timescale, indicated by the arrow. (**B**) A filament forms along the target surface in the direction of the laser pulse due to energetic electrons accelerated from coupling between the pulse and surface plasma waves. (**C**) The rapidly expanding hot electron population induces field ionization in the cold electron population of the liquid leading to a growing dark ring which surrounds the laser point where the laser is incident onto the target. (**D**) Filaments within the expanding ionization front grow due to anisotropy in the temperature distribution and are reinforced by magnetic fields initiated by the hot electron current. (**E**) Growth of the ionization front stagnates after 1.14 ps. (**F**) Recombination occurs as the plasma cools, shrinking the darkened patch. (**G**) The plasma cools over a relatively long timescale (greater than 100 ps). (**H**) Filaments persist at late times likely due to non-uniform heating caused by the radial instability.

is a repeatable process seeded by an anisotropy that does not significantly vary across shots. Since the Weibel instability arises from an anisotropy in the momentum distribution of electrons, the laser polarization and shape of the laser focal spot at the target are likely sources. In order to test this, a movie was generated at a *fixed* time delay of 1 ps when the filamentary structures are at time of maximum expansion, but over a set of shots in which the laser beam itself was perturbed by placing a 1 mm diameter wire into the laser beam before entering the target chamber. When the wire was placed in the beam, the radial filaments' angles were found to change as observed in the movie. It was also observed that motion of the wire caused the filaments to move, while if the wire was held obstructing but stationary, the filaments maintained their new orientations. Finally, the original filament structure was reestablished when the wire was removed. This leads us to conclude that the filaments are seeded by higher order terms in the laser mode which modify the laser focus at the target. Figure 3 displays the variation in the filament structure observed in the movie and the actual movie generated is contained in the supplement.

Polarization dependence of the filament structure was also studied to ascertain if the filamentation is determined primarily by the lower intensity wings of the laser focus or is induced by the hot electron dynamics dependant on the laser coupling and polarization. Movies were recorded with *s*- and *p*- polarized light through the use of a half waveplate placed in the beam before entry into the vacuum chamber. The ionization patches for linear polarization cases are shown in Fig. 4. The radial extent of the ionized region changes though the intensity is constant, so the ionized region cannot be exclusively attributed to radial intensity distribution of the laser focus. As the polarization was changed from *p*- (maximum laser coupling) to *s*- (minimum laser coupling)[31] the size of the ionization patch shrunk and the filament length decreased though preserving a similar overall structure. These results indicate, for this experiment, the radial range of relativistic electron expansion is greater than the diameter at which the intensity of the focus is below the ionization threshold. We should note that previous work by Haffa *et al.*[6] ascribes the dependence of the spatial extent of the ionization front primarily on the laser focus mode, stating that the hot electron expansion contribution cannot be ruled out. One potential possibility is the relevant laser modes for Haffa *et al.* generate relativistic electrons in the peak intensity which do not propagate significantly beyond the region directly ionized by the laser.

Recombination. About one picosecond after the first features on shadowgraphy appear, the ionization patch stops growing, and maintains its size for about 80 to 90 picoseconds, after which the darkened background begins to disappear. The disappearance occurs from the outer edges (further radial distance from the center) and inward,

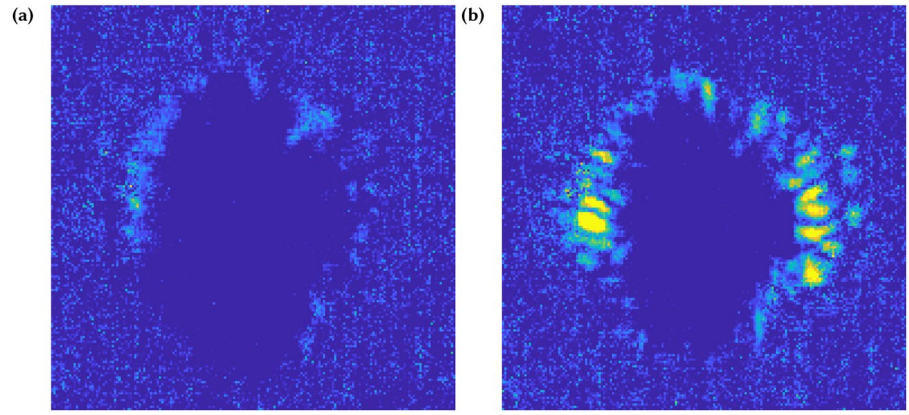

Figure 3. Arbitrarily unit pseudo-color plots of the local shot-to-shot variation of shadowgraphs of the expanded plasma at 1 ps delay. A video, provided in the Supplemental Data, is of a series of individual RLPI interactions perturbed by passing a wire through the compressed, collimated pump. Plotted here is the cumulative pixel-by-pixel difference of sequential shadowgraphic frames, with yellow-to-green representing a larger sum, or more local shot-to-shot variation. (**a**) demonstrates the stable control case with no wire obstruction and (**b**) shows the shadowgraphy variation when a wire is perturbing the mode.

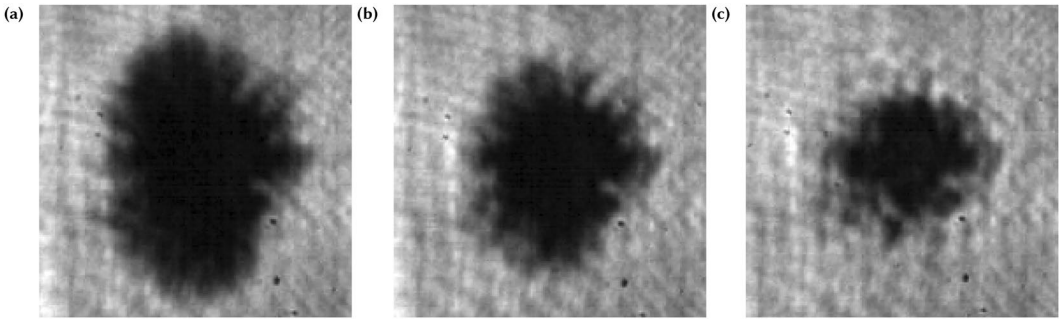

Figure 4. Shadowgraphic images (from provided video) with a 1 ps probe delay of experiments with identical laser parameters (see text) including energy and mode with incident (**a**) *p*-polarization, (**b**) 45°, and (**c**) *s*-polarization. The disparity in the extent of ionization between *p*- and *s*- polarization implies that the shape of the ionization feature is and is not exclusively dependent on the laser mode. It should be noted that experiments on a different system, attributes the dependence to the laser mode shape[6].

giving the appearance of shrinking. During this shrinking, the darkening decreases, making the filaments more apparent, although the edges of the filaments do also begin to vanish as well. This we interpret as occurring due to electron-ion recombination, and thus these movies serve as a probe of the electron-ion recombination rate for high density plasma. Finally 200 picoseconds after the initial laser interaction, the dark patch has reduced to a spot smaller than 30 microns, where it remains that size until the 300–400 picoseconds where the material begins to explode.

Simulations. The three-dimensional Particle-in-Cell (PIC) simulation using the Large-Scale Plasma (LSP) code[32] was employed in order to model this experiment and help elucidate the mechanism responsible for the filaments. Given the geometry of the experiment, lower dimensional simulations would not capture the full dynamics of the ionization correctly. This computationally expensive simulation was designed to closely follow the actual experiment, the details can be found in the Methods section.

As discussed previously and shown in Fig. 1c, the filaments develop within femtoseconds of the laser interacting with the target as can be seen in videos of the simulation included in the supplement. First the laser irradiates the spot, creating an ionization patch the shape of the laser projected onto the target. After approximately 30 fs, a well defined ionization front propagates at $0.77c$ radially away from the spot, where c is the speed of light. There is a variation in the free electron density behind this front as a function of position in the thickness of the target, in which the back surface and front surface of the target are higher density ($\sim 10^{22}$ cc^{-1}) with the center of the target well below the critical density of the probe which is $6.9 \cdot 10^{21}$ cc^{-1}. Behind this front, another region of higher density expands outward radially at a slower speed of about $0.34c$. This high density region is characterized by the protons being ionized and the carbon and oxygen atoms ionized to the K-shell. Behind the edge of this region, filaments are found to form. These filaments are radially directed, in agreement with the experiment, with random pitch to the filaments through the thickness of the target, as shown in Fig. 5b,d. For reasons discussed below, a

one-to-one comparison cannot be made between the experimental shadowgraphy and the simulation's final electron plasma density when the whole simulation box's target is ionized. Nonetheless, the speed of the expansion of the high density region in the simulations is found to agree with the earliest observed speed of the shadowgraph's growth, which we measure in the verticle direction to be $0.4c$.

Ionization variation in the target. In addition to the most stark feature of the filaments, there is a variation in the evolution of free electron density through the thickness of the target, which is shown in Fig. 5 and along the x-axis as shown in the inset of that figure. The variation can be classified by considering layers of the target through the thickness of the target along the x-axis, which are well resolved given the 10 nm cell sizes utilized in this simulation. The general trend is the front and back surfaces are more ionized compared to bulk thickness of the target, as shown in (b), with (a) showing the back is ionized to a higher degree. As previously discussed, outside of the initial irradiation of the spot, the density behind the fast ionization front is less than the critical density of the probe and thus difficult to observe experimentally.

There does exist some structure in the ionization as a function of radius and x position beyond the general trend of ionization of the surfaces. One feature found from inspection of Fig. 5 is on the front side shown in (c) at a radius just beyond the filaments, the ionization is low but then increases at a larger radius. This is both shown in (c) as the lower density shadow just on the right of the filaments and in the plot of the density through the x-axis (b) by examining the volume between the dotted lines at $-0.23\,\mu$m and $-0.1\,\mu$m. Furthermore, the plot of the front layer (c) shows that this feature has an ellipsoidal symmetry in the target plane. Upon further examination of Fig. 5b, there is also a general higher density layer between $x = 0.0\,\mu$m and $x = 0.1\,\mu$m near the back of the target which only extends to a radius of $17\,\mu$m. When viewed as a layer in a manner similar to (a) and (c) but not shown here, it appears as a disc. Finally, the back side of the target shown in Fig. 5a is almost completely ionized to a high degree, as discussed in the previous paragraph, with the highest ionization being the filaments and the shadow of the spot. Most of the ionization shown in the in (a) is due to the ionization in the last few cells of the target region being highly ionized.

Comparison of simulations and the experiment. As noted previously the filamentation in the simulation occurs within femtoseconds, while the laser is still reflecting off the target. In the experimental shadowgraphy, the filaments only become apparent well after ~100 fs, on picosecond timescales after the initial RLPI. Because of the computational expense of 3D PIC simulations, we are unable to simulate this phenomena beyond 100 fs and over a larger target and cannot perform a one-to-one comparison between the simulations and the experiment. However, we believe that it is very likely that the instability is seeded during the laser interaction as the simulations suggest. However, the very initial ionization is not directly observable experimentally. It is valuable to remind the reader that the simulations only capture the first 100 fs after the laser reaches the target which is comparable to the 80 fs FWHM of the probe illumination, making it difficult for the very initial ionization process to be captured by the probe.

We currently do not have the capability to experimentally measure the magnetic field strength or distribution on the target as a validation for the magnetic field distribution that develops in the simulation (e.g.[33]). Nonetheless, it is very likely that the Weibel instability observed in our simulation is the seed of the filaments observable a picosecond later in the shadowgraphy, and these larger filaments could still be due to the Weibel instability. Though the PIC simulation develops nanometer-scale filaments, as hot electrons transport and expand away from the focal spot, the hot electron density, and corresponding wavenumber of the Weibel instability[13,34], will drop for larger radii. We thus propose the initial filaments expand, diffuse over time (similar to Scott *et al.*[19]), and are ultimately observable in the shadowgraphy.

Finally, in an attempt to compare the simulation to the experiment more directly, a synthetic "shadowgraphy" from the simulation was created to compare to the experimental videos. This was done by taking into account the attenuation using a simple Lambert-Beer's law using the density of the plasma in the simulation as well as convolving with the finite duration of the probe pulse. It was found that up until the end of the simulation the filaments do not appear and only the shadow of the laser spot is visible. Nonetheless, it is assumed that these initial filaments grow in size as the ionization patch grows, after which they become visible experimentally, in the manner discussed above.

Impact of this observation. Finally, it is worth speculating about the implications of this observation. Instabilities have been found to be present in a host of experiments with high intensity laser experiments (including RLPI), and we can add this particular flavor of instability, filamentation of the surface plasma due to anisotropy in the laser mode to the battery of instabilities one would expect in laser plasma interactions. In addition to instabilities like Rayleigh-Taylor and others, it is conceivable that this instability would particularly affect reduced mass targets[35,36] that are used for either ion acceleration or as candidates for warm dense matter studies, and this instability could lead to inhomogeneities in the heating of the latter. For example, with the advent of PW class lasers, significant RLPI experiments are moving into ultrathin targets (10–100 nm), where radial instabilities may play a significant role in determining the spectra and mode of ion acceleration. Another aspect is that a new thrust in RLPI physics is to study the dense plasma interaction with non-conventional polarization states[37,38]. With regards to ion acceleration, the traditional Weibel filamentation along the direction of laser propagation[39] affects the mode of the accelerated ions. The radial instability observed in this work is potentially responsible for the radial striations found in lower energy proton spatial distributions of TNSA expansions from 1 micron thick solid targets[27], not typically present in the central and higher energy protons. It is conceivable that in TNSA experiments with higher intensity lasers (intensities exceeding 10^{20} W/cm^2), the high intensities would drive stronger currents leading to more susceptibility to instabilities like that observed here. However, it was in fact observed in the simulations that just in and around the laser spot does not display radial filamentation, as the

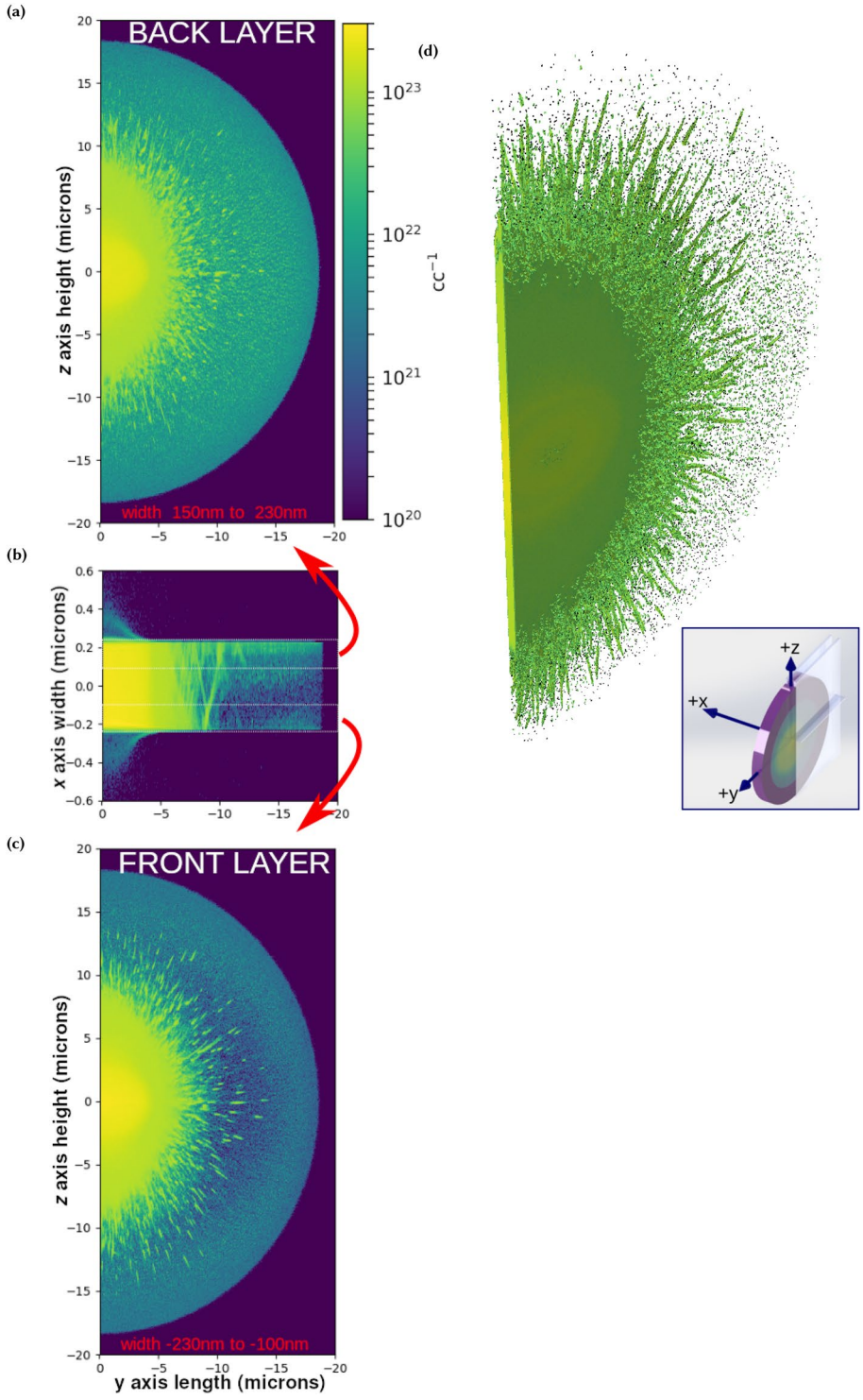

Figure 5. Sub-figures (**a**) to (**c**) show the free electron density variation through the thickness of the target, or the *x*-axis as shown in the inset, and highlight general trends in the density variation. All figures consider the target density away from the laser forward direction, which is along the negative-*y* axis. (**b**) shows the free electron density averaged over half a micron in the transverse direction (*z*-axis), with the vertical dimension of the figure corresponding to the *x*-axis expanded to show detail. (**a**) shows the electron density on the back surface of the target, averaged 80 nm along the *x*-axis and (**c**) shows the front of the target averaged through 130 nm along the *x*-axis. (**b**) also shows, although distorted due to the expansion of vertical dimension, the random pitch of the filaments through the thickness axis of the target. (**d**) shows a volumetric three dimensional render of this half of the target which further highlights the orientation of the filaments. See the inset for convienience in understanding the orientation of these plots, in which the volumes displayed in (**a**) to (**c**) are highlighted by the semi-transparent rectangles shown. The color map for these figures is the same as that for Fig. 1c. This figure was produced using Matplotlib[46] and Mayavi[47].

radial filamentation only occurs when hot electrons begin to leave the laser spot. Therefore, one potential mitigation of this instability in reduced mass target experiments is to ensure the target is about the size of the laser spot in area by defocusing the beam.

Methods

Experimental setup. The experiment, displayed in Fig. 1a, was performed with a heavily modified dual multi-pass amplifier Ti:Sapphire KMLabs Red Dragon laser system which generates 40 fs (FWHM) pulses at 780 nm wavelength with up to 5 mJ of short pulse energy reaching the target, focused by an F/1 protected gold coated off axis paraboloid, creating a 1.8 μm diameter (FWHM) spot. Pulses were focused at a 45 degree angle of incidence on to the target which was a freely suspended, sub-micron (~0.5 μm) thin sheet of ethylene glycol formed by the off-center collision of two liquid jets[40]. Despite the use of a liquid target flowing at 24 ms^{-1}, the vacuum chamber pressure was maintained to less than 50 μbar during operation. For this system the non-linear effects on the mode propagating through focus are not observed below 55 mbar. The laser-target interaction was illuminated by means of a short pulse probe beam created from amplifying the longer wavelength portion of different pulses of a common oscillator then is frequency doubled to produce 420 nm probe allowing the 390 nm second harmonic emission from the RLPI to be filtered out as described in the Feister *et al.*[10]. The use of a common oscillator allows for optical synchronization of the shadowgraphic probe with the pump pulse. To calibrate the relative time delay between the pump and the probe, we reduce the intensity of the main (i.e. pump) pulse to the point where it just ionizes the target (as visible in the shadowgraphy). This allows the timing of the probe relative to the pump to be determined within the ~80 fs (FWHM) duration of the probe pulse and 100 fs step size of the delay stage. This approach was used to determine the times in Fig. 2 panel B, which presents shadowgraphy at $+100 \pm 100$ fs and -220 ± 100 fs time delay.

Utilizing the repetition rate, we develop time resolved movies of the target evolution in the following way: for a given time delay, ten acquisitions of shadowgraphs are averaged. Then, out of the ten, the shadowgraph closest in total value to the average is chosen as the shadowgraph for this delay. This process is repeated across a number of delays to create the time resolved movie. To acquire a movie in a reasonable length of time, and roughly follows the natural time scales of the dynamics, the delays are chosen such that the time between frames increases cubically starting a picosecond after the initial interaction. It should be noted that data presented in a typical 400 frame movie represents ~4000 acquisitions during ~120 thousand relativistic interactions, demonstrating the significance of high repetition rate experimental platforms in studying RLPI with solid density targets.

Simulations. Due to the geometry of the target and the the ionization region, a three-dimensional PIC simulation was performed. This large scale simulation required 5632 cores, pushing well into the tera-FLOP regime in terms of peak possible performance. The simulation had a high spatial resolution of 10 nm cells through the thickness of the target, 25 nm and 50 nm along the axis along the polarization axis and along the axis normal to the polarization plane respectively, which allowed detailed observation of the RLPI. The target had a thickness of 460 nm with a height of 40 μm and width of 40 μm at a density of $1.08 \cdot 10^{22}$ cc^{-1}, to closely follow the actual target. In this simulation the laser was a 42 fs $5 \cdot 10^{18}$ W/cm^2 pulse with a 1.87 μm spatial Gaussian radius incident at a 45 degree incidence angle to the target with *p*-polarization. The focus of the pulse was placed at the target surface.

The number of atoms per cell is 8 per species, however, given the high spatial resolution of the simulation, this is not considered to be too low compared to other high fidelity three-dimensional simulations (for example, see Sentoku *et al.*[12]). The starting temperature was room temperature (0.025 eV) with atomic species; given the species were started neutral (without a plasma), the regions of the target would not be susceptible to grid heating[41] before ionization. The simulation employs a field ionization model that follows the PPT/ADK rate[42,43] and allows for Coulomb collisions once regions of the target are ionized that follow the Spitzer rate[44].

The absorbing boundary conditions used[45] are not ideal and we observed reflection of an amount of laser light three orders down in intensity off these boundaries which re-intersect the target. Light transmitted through the target and is re-incident makes a negligible contribution to the free electron density as the intensity is much lower than the incident light. The significant front surface reflection intersects with the target away from the initial laser focus after the relativistic electron expansion has passed. This second interaction occurs after the filaments have formed and was not observed to impact their evolution at late times, particularly for the target ionization on the opposite side of the laser direction (negative horizontal dimension in Fig. 1c and negative *y*-axis in the inset of Fig. 5).

Data availability

Additional experimental data generated in this study and not already provided in the Supplemental Data will be given upon a reasonable request. The LSP code is not freely available, and access to it should be discussed with Voss Scientific, Albuquerque, NM. However, if one has access to the code, the input files to perform the simulations utilized here can be given upon reasonable request of the corresponding author.

Received: 25 December 2019; Accepted: 18 May 2020;
Published: 18 June 2020

References

1. Strickland, D. & Morou, G. Compression of amplified chirped optical pulses. *Opt. Commun.* **55**, 447–449, https://doi.org/10.1016/0030-4018(85)90151-8 (1985).
2. Wilks, S. *et al.* Energetic proton generation in ultra-intense laser–solid interactions. *Phys. plasmas* **8**, 542–549 (2001).
3. Tajima, T. & Dawson, J. M. Laser Electron Accelerator. *Phys. Rev. Lett.* **43**, 267–270 (1979).

4. Morrison, J. T. *et al*. Backward-propagating mev electrons from 1018 w/cm2 laser interactions with water. *Phys. Plasmas* **22**, 043101 (2015).
5. Orban, C. *et al*. Backward-propagating MeV electrons in ultra-intense laser interactions: Standing wave acceleration and coupling to the reflected laser pulse. *Phys. Plasmas* **22**, 1405.6313, https://doi.org/10.1063/1.4913225 (2015).
6. Haffa, D. *et al*. Temporally resolved intensity contouring (tric) for characterization of the absolute spatio-temporal intensity distribution of a relativistic, femtosecond laser pulse. *Sci. Reports* **9**, 697, https://doi.org/10.1038/s41598-019-42683-z (2019).
7. Borghesi, M. *et al*. Proton imaging detection of transient electromagnetic fields in laser-plasma interactions (invited). Rev. *Sci. Instruments* **74**, 1688–1693, https://doi.org/10.1063/1.1534390 (2003).
8. Li, C. K. *et al*. Monoenergetic proton backlighter for measuring e and b fields and for radiographing implosions and high-energy density plasmas (invited). *Rev. Sci. Instruments* **77**, 10E725, https://doi.org/10.1063/1.2228252 (2006).
9. Liao, G. *et al*. Proton radiography of magnetic fields generated with an open-ended coil driven by high power laser pulses. *Matter Radiat. at Extrem.* **1**, 187–191, https://doi.org/10.1016/j.mre.2016.06.003 (2016).
10. Feister, S. *et al*. A novel femtosecond-gated, high-resolution, frequency-shifted shearing interferometry technique for probing pre-plasma expansion in ultra-intense laser experiments. *Rev. Sci. Instruments* **85**, https://doi.org/10.1063/1.4886955 1406.3639 (2014).
11. Weibel, E. S. Spontaneously growing transverse waves in a plasma due to an anisotropic velocity distribution. *Phys. Rev. Lett*. **2**, 83–84, https://doi.org/10.1103/PhysRevLett.2.83 *arXiv:1011.1669v3* (1959).
12. Sentoku, Y. *et al*. Three-dimensional particle-in-cell simulations of energetic electron generation and transport with relativistic laser pulses in overdense plasmas. *Phys. Rev. E - Stat. Physics, Plasmas, Fluids, Relat. Interdiscip. Top.* **65**, 7, https://doi.org/10.1103/PhysRevE.65.046408 (2002).
13. Sentoku, Y., Mima, K., Kojima, S. I. & Ruhl, H. Magnetic instability by the relativistic laser pulses in overdense plasmas. *Phys. Plasmas* **7**, 689–695, https://doi.org/10.1063/1.873853 (2000).
14. Wallace, J. M., Brackbill, J. U., Cranfill, C. W., Forslund, D. W. & Mason, R. J. Collisional effects on the Weibel instability. *Phys. Fluids* **30**, 1085, https://doi.org/10.1063/1.866305 (1987).
15. Honda, M., Meyer-Ter Vehn, J. & Pukhov, A. Collective stopping and ion heating in relativistic-electron-beam transport for fast ignition. *Phys. Rev. Lett.* **85**, 2128–2131, https://doi.org/10.1103/PhysRevLett.85.2128 (2000).
16. Tatarakis, M. *et al*. Measurements of ultrastrong magnetic fields during relativistic laser-plasma interactions. *Phys. Plasmas* **9**, 2244–2250, https://doi.org/10.1063/1.1469027 (2002).
17. Califano, F., Del Sarto, D. & Pegoraro, F. Three-dimensional magnetic structures generated by the development of the filamentation (Weibel) instability in the relativistic regime. *Phys. Rev. Lett.* **96**, 1–4, https://doi.org/10.1103/PhysRevLett.96.105008 (2006).
18. Tatarakis, M. *et al*. Propagation Instabilities of High-Intensity Laser-Produced Electron Beams. *Phys. Rev. Lett.* **90**, 4, https://doi.org/10.1103/PhysRevLett.90.175001 (2003).
19. Scott, G. G. *et al*. Diagnosis of weibel instability evolution in the rear surface density scale lengths of laser solid interactions via proton acceleration. *New J. Phys.* **19**, 043010, https://doi.org/10.1088/1367-2630/aa652c (2017).
20. Quinn, M. N. *et al*. On the investigation of fast electron beam filamentation in laser-irradiated solid targets using multi-MeV proton emission. *Plasma Phys. Control. Fusion* **53**, 124012, https://doi.org/10.1088/0741-3335/53/12/124012 (2011).
21. MacLellan, D. *et al*. Fast electron transport patterns in intense laser-irradiated solids diagnosed by modeling measured multi-mev proton beams. *Laser Part. Beams* **31**, https://doi.org/10.1017/S0263034613000529 (2013).
22. Schoeffler, K. M. & Silva, L. O. General kinetic solution for the biermann battery with an associated pressure anisotropy generation. *Plasma Phys. Control. Fusion* **60**, 014048, https://doi.org/10.1088/1361-6587/aa883a (2017).
23. Schoeffler, K. M., Loureiro, N. F., Fonseca, R. A. & Silva, L. O. Magnetic-field generation and amplification in an expanding plasma. *Phys. Rev. Lett.* **112**, 175001, https://doi.org/10.1103/PhysRevLett.112.175001 (2014).
24. Schoeffler, K. M., Loureiro, N. F., Fonseca, R. A. & Silva, L. O. The generation of magnetic fields by the biermann battery and the interplay with the weibel instability. *Phys. Plasmas* **23**, 056304, https://doi.org/10.1063/1.4946017 (2016).
25. Shukla, N. *et al*. Interplay between the weibel instability and the biermann battery in realistic laser-solid interactions 1907.10433 (2019).
26. Quinn, K. *et al*. Weibel-induced filamentation during an ultrafast laser-driven plasma expansion. *Phys. Rev. Lett.* **108**, 135001, https://doi.org/10.1103/PhysRevLett.108.135001 (2012).
27. Wagner, F. *et al*. Maximum proton energy above 85 mev from the relativistic interaction of laser pulses with micrometer thick ch2 targets. *Phys. Rev. Lett.* **116**, 205002, https://doi.org/10.1103/PhysRevLett.116.205002 (2016).
28. George, K. M. *et al*. High-repetition-rate (>khz) targets and optics from liquid microjets for high-intensity laser–plasma interactions. *High Power Laser Sci. Eng.* **7**, e50, https://doi.org/10.1017/hpl.2019.35 (2019).
29. Wei, M. S. *et al*. Observations of the filamentation of high-intensity laser-produced electron beams. *Phys. Rev. E - Stat. Physics, Plasmas, Fluids, Relat. Interdiscip. Top.* **70**, 6, https://doi.org/10.1103/PhysRevE.70.056412 (2004).
30. Göde, S. *et al*. Relativistic electron streaming instabilities modulate proton beams accelerated in laser-plasma interactions. *Phys. Rev. Lett.* **118**, 194801, https://doi.org/10.1103/PhysRevLett.118.194801 (2017).
31. Gibbon, P. Short Pulse Laser Interactions with Matter, 10.1142/p116 (PUBLISHED BY IMPERIAL COLLEGE PRESS AND DISTRIBUTED BY WORLD SCIENTIFIC PUBLISHING CO., 2005).
32. Welch, D. R., Rose, D. V., Clark, R. E., Genoni, T. C. & Hughes, T. P. Implementation of an non-iterative implicit electromagnetic field solver for dense plasma simulation. *Comput. Phys. Commun.* **164**, 183–188, https://doi.org/10.1016/j.cpc.2004. 06.028 (2004).
33. Chatterjee, G. *et al*. Micron-scale mapping of megagauss magnetic fields using optical polarimetry to probe hot electron transport in petawatt-class laser-solid interactions. *Sci. Reports* **7**, 8347, https://doi.org/10.1038/s41598-017-08619-1 (2017).
34. Silva, L. O., Fonseca, R. A., Tonge, J. W., Mori, W. B. & Dawson, J. M. On the role of the purely transverse weibel instability in fast ignitor scenarios. *Phys. Plasmas* **9**, 2458–2461, https://doi.org/10.1063/1.1476004 (2002).
35. Neumayer, P. *et al*. Isochoric heating of reduced mass targets by ultra-intense laser produced relativistic electrons. *High Energy Density Phys.* **5**, 244–248, https://doi.org/10.1016/j.hedp.2009.05.009 (2009).
36. Tresca, O. *et al*. Controlling the properties of ultraintense laser–proton sources using transverse refluxing of hot electrons in shaped mass-limited targets. *Plasma Phys. Control. Fusion* **53**, 105008 (2011).
37. Jeong, T. M., Bulanov, S. B., Weber, S. W. & Korn, G. Analysis on the longitudinal field strength formed by tightly-focused radially-polarized femtosecond petawatt laser pulse. *Opt. Express* **26**, 33091–33107 (2018).
38. Rykovanov, S. G. *et al*. Ion acceleration with ultra-thin foils using elliptically polarized laser pulses. *New J. Phys*. **10**, https://doi.org/10.1088/1367-2630/10/11/113005 (2008).
39. Metzkes, J. *et al*. Experimental observation of transverse modulations in laser-driven proton beams. *New J. Phys.* **16**, 023008 (2014).
40. Morrison, J. T. *et al*. MeV proton acceleration at kHz repetition rate from ultra-intense laser liquid interaction MeV proton acceleration at kHz repetition rate from ultra-intense laser liquid interaction. *New J. Phys*. **20** (2018).
41. Langdon, A. B. Effects of the spatial grid in simulation plasmas. *J. Comput. Phys*. **6**, 247–267, https://doi.org/10.1016/0021-9991(70)90024-0 (1970).
42. Perelomov, A. M., Popov, V. S. & Terent'ev, M. V. Ionization of atoms in an alternating electrical field. *Sov. Phys. JETP* **23**, 924 (1966).
43. Ammosov, M. V., Delone, N. B. & Krainov, V. P. Tunnel ionization of complex atoms and of atomic ions in an alternating electromagnetic field. *Sov. Phys. JETP* **64**, 1191–1194, https://doi.org/10.1117/12.938695 (1986).
44. Spitzer, L. Physics of Fully Ionized Gases. *Am. J. Phys.* **31**, 890–891, https://doi.org/10.1119/1.1969155 (1963).

45. Mur, G. Absorbing Boundary Conditions for the Finite-Difference Approximation of the Time-Domain Electromagnetic-Field Equations. *IEEE Transactions on Electromagn. Compat. EMC* **23**, 377–382, https://doi.org/10.1109/TEMC.1981.303970 (1981).
46. Hunter, J. D. Matplotlib: A 2d graphics environment. *Comput. Sci. & Eng.* **9**, 90–95, https://doi.org/10.1109/MCSE.2007.55 (2007).
47. Ramachandran, P. & Varoquaux, G. Mayavi: 3D Visualization of Scientific Data. *Comput. Sci. & Eng.* **13**, 40–51 (2011).

Acknowledgements

This work was performed at AFRL at WPAFB supported by the Air Force Office of Scientific Research under LRIR Project 17RQCOR504 managed by Dr. Riq Parra. Moreover, this research was performed while the author G.K.N. held an NRC Research Associateship award at the Air Force Research Laboratory, Dayton, O.H.

Author contributions

W.M.R., E.A.C. and C.O. provided leadership and oversight for the experimental and simulation effort. J.T.M. and K.M.G. conducted the experiments and performed analysis with E.A.C., supported by K.D.F.'s experimental setup, maintenance, and automation without which this work is not possible and G.K.N. performed the simulations and comparisons to the experimental result. J.R.S. helped with writing and proofreading the manuscript. All authors reviewed, edited, and contributed to the manuscript.

Competing interests

The authors declare no competing interests.

Additional information

Supplementary information is available for this paper at https://doi.org/10.1038/s41598-020-66615-4.

Correspondence and requests for materials should be addressed to G.K.N.

Reprints and permissions information is available at www.nature.com/reprints.

Publisher's note Springer Nature remains neutral with regard to jurisdictional claims in published maps and institutional affiliations.